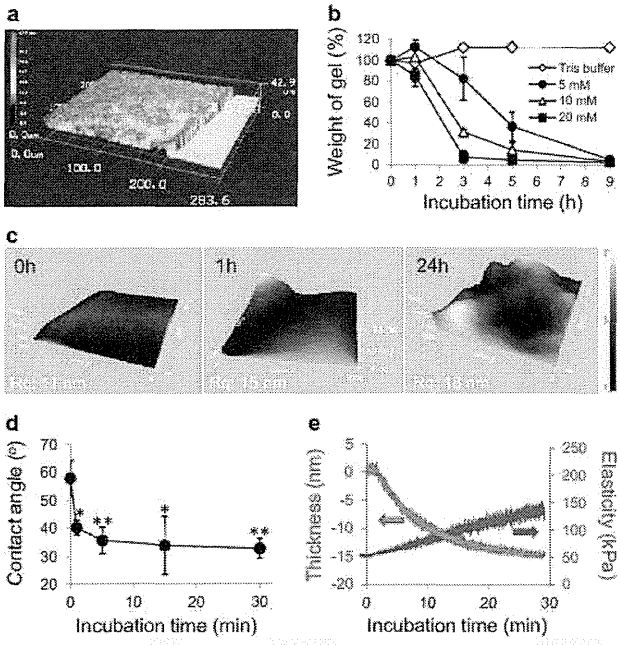

Figure 2. a) Laser microscopic image of γ-PGA-SS 6–1–1 gel film under semi-wet conditions. b) The weight loss of gel films during the incubation with 0×10^{-3}, 5×10^{-3}, 10×10^{-3}, and 20×10^{-3} M of cysteine/50×10^{-3} M Tris-HCl solution (pH 7.4) at 37 °C ($n = 3$). γ-PGA-SS gel films prepared on Au substrate was immersed in cysteine solution for 9 h incubation. Weights were calculated from results of QCM analyses. c) AFM images of gel film surfaces exposed to 20×10^{-3} M of cysteine for 0, 1, and 24 h. The quadratic mean roughness (*Rq*) was calculated from AFM analyses. d) Dynamic change in contact angles of gel films during 20×10^{-3} M of cysteine exposure. Contact angles were measured within 10 s after water drop. * $P < 0.05$, ** $P < 0.01$ when compared with 0 h, Student's *t*-test ($n = 3$). e) QCM-D analysis for measuring thickness and elasticity of gel film exposed to 20×10^{-3} M cysteine. These results were calculated by viscoelastic analyses.

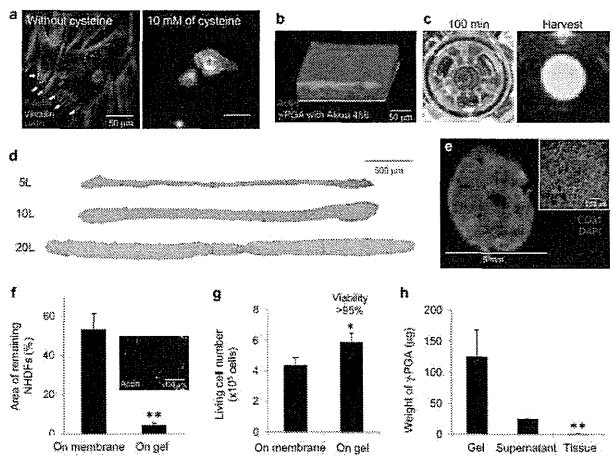

Figure 3. a) CLSM images of actin fibers and focal adhesion staining of cells on gel films without and with 10×10^{-3} M cysteine for 1 h. Arrows denote the expressions of vinculin. b) 3D-reconstructed CLSM image of NHDF-tissues constructed on γ-PGA-SS gel films. NHDFs were stained with Rhodamine-phalloidine and γ-PGA polymers were labeled with Alexa 488. c) 5L-NHDF tissues after incubation with cysteine-containing media at 37 °C for 100 min and after detachment from gel films by gentle pipetting. d) HE images of 5L-, 10L-, and 20L-NHDF tissues harvested from gel films. e) Reconstructed CLSM image of a blood-capillary model harvested from the substrate. HUVECs were immunostained with anti-CD31 antibodies and nuclei were stained with DAPI. f) The area of remaining NHDFs on the substrate. The area was estimated from CLSM images. g) Living cell number in 5L-NHDF tissues after harvesting from membrane and gel films. h) The remaining weight of γ-PGA polymers in gel films, supernatants, and tissues after 1 h of incubation with and without cysteine. Fluorescently labeled γ-PGA polymers were used for measurements of polymer weight. * $P < 0.05$, ** $P < 0.01$ when compared with the other samples, Student's *t*-test ($n = 3$).

10×10^{-3} M cysteine, NHDFs began to change morphology to spherical shapes within 10 min and almost all cells detached after few hours (Figure S7 and Movie 1, Supporting Information). The cysteine itself did not affect cellular morphology up to a 10×10^{-3} M concentration (Figure S7a, Supporting Information). Moreover, cytoskeletal structures including actin filaments and vinculin that organizes adhesion maturation through the linkage of integrin molecules to actin filaments in focal adhesion[15] were observed by confocal laser scanning microscopy (CLSM) (**Figure 3**a). These expressions significantly decreased after exposure to cysteine in 1 h. As disulfide bonds are cleaved, the hydrophilicity and roughness on gel surfaces increases which weakens interactions with gels and proteins, especially coated fibronectin. The weakened mechanical feedback from interactions between the dynamic nano-interfaces and integrin molecules may cause immature adhesion and cytoskeletal remodeling, leading to sequential detachment of cells.

Based on these results of cellular detachment at the single-cell level, we addressed harvesting 3D tissues from substrates. The 3D-multilayered tissues comprising NHDFs were constructed onto γ-PGA-SS 6–1–1 gel films by a cell-accumulation technique (Figure 3b and Figure S8, Supporting Information). The five-layered- (5L-) tissues were harvested by exposure with 5×10^{-3} M cysteine and gentle pipetting. After 100 min of incubation with cysteine, tissues detached from the edge of membranes to decrease the adhesion area to half and harvested by sequential gentle pipetting, and there was no change in tissues directly constructed on membranes (without gel films) (Figure 3c and Figure S9a, Supporting Information). Histological observations of tissues on membranes, which were physically separated by scraping with tweezers, displayed defects and much cellular debris (Figure S9b, Supporting Information), while gel films allowed for harvesting homogeneous tissue structures without defects and the various layer number of tissues can be harvested (Figure 3d), except 1L of tissues with

weak mechanical properties (less than 5 μm in thickness) (Figure S10, Supporting Information). Besides, more functional tissues such as blood-capillary models with human umbilical vein endothelial cells (HUVECs),[16] liver tissues of HepG2, and heart tissues of iPS-derived cardiac myoblast cells were harvested using gel films (Figure 3e and Figure S11, Supporting Information). These tissues revealed specific functionalities including the production of albumin and the cardiac pulsation over more than 1 month (Movie 2, Supporting Information). Even after the harvesting process, the obtained tissues possessed ECM proteins (fibronectin) unlike the use of degrading enzymes (Figure S12, Supporting Information). Moreover, many remaining cells were observed on membranes in the physically scraped sample (Figure 3f and Figure S13, Supporting Information), while samples using gel films revealed high cell viability (>95%) and high yield after harvesting (Figure 3g). Since this method does not require drastic changes in culture environments such as decreases in temperature,[8] photoirradiation,[7a,b] and low pH,[7c] physical and chemical damage were considered to decrease. More importantly, few γ-PGA polymers were detected in tissues after the degradation process (Figure 3h), because remaining polymers such as poly(lactic acid)s may induce the inflammatory side reaction due to carboxylic groups during degradation process.[17]

In conclusion, we presented a novel and versatile technique for harvesting functional 3D-engineered tissues using stimuli-responsive γ-PGA-SS gel films with dynamic nano-interfaces. We found that the surface properties of gel films including mainly wettability and roughness were dynamically controlled in response to reducing amino acids. This dynamic hydrophobic to hydrophilic change on nano-interfaces allowed for cellular detachment at the single-cell level and the harvesting of 3D-engineered tissues through the control of cell–material interactions. Tissues can be harvested with high efficiency upon exposure to cysteine without serious physical damage and maintain ECM proteins. Functional 3D tissues that recreated blood capillary, liver, and cardiac tissue were also obtained and their functionalities were maintained. This simple and intact harvesting technique of 3D tissues in vitro has enormous potential as a tissue transplantation therapy to treat serious diseases such as organ failure and ischemic heart disease in regenerative medicine.

Supporting Information

Supporting Information is available from the Wiley Online Library or from the author.

Acknowledgements

This work was supported by the NEXT Program (LR026), Grant-in-Aid for Scientific Research (S) (A232250040), the SENTAN-JST Program (13A1204), a Health Labor Sciences Research Grant from the Japanese Ministry of Health, Labor, and Welfare, and Grand-in-Aid for JSPS Fellows (24?622). The authors also thank S. Nishimura in MEIWAFOSIS Co., Ltd., for QCM-D analysis, A. Kimura for her technical assistance of immunohistochemistry experiments, and Y. Amano for preparation of iPS-derived cardiac myoblast tissue.

Received: January 28, 2015
Revised: MM DD, YYYY
Published Online: MM DD, YYYY

[1] a) S. Rafii, D. Lyden, *Nat. Med.* **2003**, *9*, 702; b) S. Yamanaka, *Cell Stem Cell* **2007**, *1*, 39; c) K. Takahashi, K. Tanabe, M. Ohnuki, M. Narita, T. Ichisaka, K. Tomoda, S. Yamanaka, *Cell* **2007**, *131*, 861; d) D. A. Robinton, G. Q. Daley, *Nature* **2012**, *481*, 295.

[2] V. F. M. Segers, R. T. Lee, *Nature* **2008**, *451*, 937.

[3] K. Suzuki, B. Murtuza, J. R. Beauchamp, R. T. Smolenski, A. Varela-carver, S. Fukushima, S. R. Coppen, T. A. Partridge, M. H. Yacoub, *FASEB J.* **2004**, *18*, 1153.

[4] a) R. Langer, J. P. Vacanti, *Science* **1993**, *260*, 920; b) P. X. Ma, *Mater. Today* **2004**, *7*, 30.

[5] a) H. W. Kang, Y. Tabata, Y. Ikada, *Biomaterials* **1999**, *20*, 1339; b) K. Y. Lee, D. J. Mooney, *Chem. Rev.* **2001**, *101*, 1869; c) P. M. Kharkar, K. L. Kiick, A. M. Kloxin, *Chem. Soc. Rev.* **2013**, *42*, 7335.

[6] Y. Haraguchi, T. Shimizu, M. Yamato, T. Okano, *RSC Adv.* **2012**, *2*, 2184.

[7] a) M. Wirkner, J. M. Alonso, V. Maus, M. Salierno, T. T. Lee, A. J. García, A. del Campo, *Adv. Mater.* **2011**, *23*, 3907; b) S. Yamaguchi, S. Yamahira, K. Kikuchi, K. Sumaru, T. Kanamori, T. Nagamune, *Angew. Chem.* **2012**, *124*, 132; *Angew. Chem. Int. Ed.* **2012**, *51*, 128; c) Q. An, J. Brinkmann, J. Huskens, S. Krabbenborg, J. de Boer, P. Jonkheijm, *Angew. Chem.* **2012**, *124*, 12399; *Angew. Chem. Int. Ed.* **2012**, *51*, 12233; d) H. Tan, X. Gao, J. Sun, C. Xiao, X. Hu, *Chem. Commun.* **2013**, *49*, 11554.

[8] a) A. Kushida, M. Yamato, C. Konno, A. Kikuchi, Y. Sakurai, T. Okano, *J. Biomed. Mater. Res.* **1999**, *45*, 355; b) J. Yang, M. Yamato, C. Kohno, A. Nishimoto, H. Sekine, F. Fukai, T. Okano, *Biomaterials* **2005**, *26*, 6415; c) K. Matsuura, R. Utoh, K. Nagase, T. Okano, *J. Controlled Release* **2014**, *190*, 228.

[9] Y. Akiyama, A. Kikuchi, M. Yamato, T. Okano, *Langmuir* **2004**, *20*, 5506.

[10] a) M. Matsusaki, H. Yoshida, M. Akashi, *Biomaterials* **2007**, *28*, 2729; b) H. Yoshida, M. Matsusaki, M. Akashi. *Adv. Funct. Mater.* **2013**, *23*, 1736.

[11] S. Aleksanian, Y. Wen, N. Chan, J. K. Oh, *RSC Adv.* **2014**, *4*, 3713.

[12] a) A. Nishiguchi, H. Yoshida, M. Matsusaki, M. Akashi, *Adv. Mater.* **2011**, *23*, 3506; b) M. Matsusaki, K. Kadowaki, Y. Nakahara, M. Akashi, *Angew. Chem.* **2007**, *119*, 4773; *Angew. Chem. Int. Ed.* **2007**, *46*, 4689; c) M. Matsusaki, H. Ajiro, T. Kida, T. Serizawa, M. Akashi, *Adv. Mater.* **2012**, *24*, 454.

[13] a) S. Shimomura, H. Matsuno, K. Tanaka, *Langmuir* **2013**, *29*, 11087; b) I. Tokarev, S. Minko, *Soft Matter* **2009**, *5*, 511.

[14] A. E. Nel, L. Madler, D. Velegol, T. Xia, E. M. V. Hoek, P. Somasundaran, F. Klaessig, V. Castranova, M. Thompson, *Nat. Mater.* **2009**, *8*, 543.

[15] B. D. Hoffman, C. Grashoff, M. A. Schwartz, *Nature* **2012**, *481*, 295.

[16] a) A. Nishiguchi, M. Matsusaki, Y. Asano, H. Shimoda, M. Akashi, *Biomaterials* **2014**, *35*, 4739; b) Y. Asano, A. Nishiguchi, M. Matsusaki, D. Okano, E. Saito, M. Akashi, H. Shimoda, *Microscopy* **2014**, *63*, 219.

[17] J. A. Hubbell, *Curr. Opin. Biotechnol.* **2003**, *14*, 551.

Q1 **PROD to AU: Author: Please define FT-IR.**

Biomaterials 35 (2014) 4739–4748

Contents lists available at ScienceDirect

Biomaterials

journal homepage: www.elsevier.com/locate/biomaterials

Effects of angiogenic factors and 3D-microenvironments on vascularization within sandwich cultures

Akihiro Nishiguchi [a], Michiya Matsusaki [a], Yoshiya Asano [b], Hiroshi Shimoda [b], Mitsuru Akashi [a,*]

[a] Department of Applied Chemistry, Graduate School of Engineering, Osaka University, 2-1 Yamada-oka, Suita 565-0871, Japan
[b] Department of Neuroanatomy, Cell Biology and Histology, Graduate School of Medicine, Hirosaki University, 5 Zaifu, Hirosaki 036-8562, Japan

ARTICLE INFO

Article history:
Received 27 November 2013
Accepted 31 January 2014
Available online 18 March 2014

Keywords:
Artificial tissue engineering
Angiogenesis
Cytokine
ECM (extracellular matrix)
Endothelial cell

ABSTRACT

The in vitro fabrication of vascularized tissue is a key challenge in tissue engineering, but little is known about the mechanisms of blood-capillary formation. Here we investigated the mechanisms of in vitro vascularization using precisely-controlled 3D-microenvironments constructed by a sandwich culture using the cell-accumulation technique. 3D-microenvironments controlled at the single layer level showed that sandwich culture between more than 3 fibroblast-layers induced tubule formation. Moreover, the secretion of angiogenic factors increased upon increasing the number of sandwiching layers, which induced highly dense tubular networks. We found that not only angiogenic factors, but also the 3D-microenvironments of the endothelial cells, especially apical side, played crucial roles in tubule formation in vitro. Based on this knowledge, the introduction of blood and lymph capillaries into mesenchymal stem cell (MSC) tissues was accomplished. These findings would be useful for the in vitro vascularization of various types of engineered organs and studies on angiogenesis.

1. Introduction

A current key challenge in tissue engineering is in vitro vascularization of an engineered tissue that can be employed for clinically-relevant therapies and as a drug testing model. Blood capillaries, which are composed of endothelial monolayer, pericytes and fibroblasts, maintain the metabolic activities and functions of organs through the transportation of nutrients and oxygen [1]. The introduction of these vasculatures into engineered tissues has advantages to avoid necrosis of the inner tissues and to enhance their functions through cellular signaling [2,3]. To develop functional blood capillaries, many attempts such as a 3-dimensional (3D) culture of endothelial cells in hydrogels composed of extracellular matrix (ECM) [4,5], the fixation of angiogenic factors into scaffolds [6–11], cell sheet engineering for transplantable tissues [12–14], and micro channel models with flow [15–17] have been reported. Although these systems are powerful methods to construct vascularized tissues, they need complicated devices and procedures for the vascularization, and the potential limitations to recreate both the structures and functions of living tissues in vitro still remain. This is obviously caused by a poor understanding of the mechanisms responsible for the formation of blood-capillary networks in vitro, and therefore the requirements for vascularization should be clarified, such as the microenvironments for cell culture, the species and stiffness of the surrounding tissue, and the effects of angiogenic factors secreted under hypoxia.

Recently, we developed the rapid construction of 3D-vascularized multilayered tissues by the formation of ECM nanofilms onto single surfaces using layer-by-layer assembly [18]. Less than 10 nm thickness of ECM films composed of fibronectin and gelatin (FN-G) allowed all cells to adhere to each other through interactions between the FN-G nanofilms and the cell membrane proteins to create various types of tissues such as blood vessel walls and livers [19–22]. Using this technique and a sandwich culture, highly dense and homogeneous endothelial tubular networks were formed in fibroblast tissues. We have confirmed that this blood-capillary model can work as a model to test the differentiation stages of cartilage-like tissue [23].

Here, we report the biochemical and physical effects that can induce in vitro vascularization in engineered 3D-microenvironments (Fig. 1a). Since the cell-accumulation technique is able to control the number of tissue layers, we could investigate the role of the 3D-microenvironment at the level of a single cell layer. We tested the effect of the fibroblast layer number, angiogenic factors

* Corresponding author. Tel.: +81 6 6879 7356; fax: +81 6 6879 7359.
E-mail address: akashi@chem.eng.osaka-u.ac.jp (M. Akashi).

http://dx.doi.org/10.1016/j.biomaterials.2014.01.079
0142-9612/

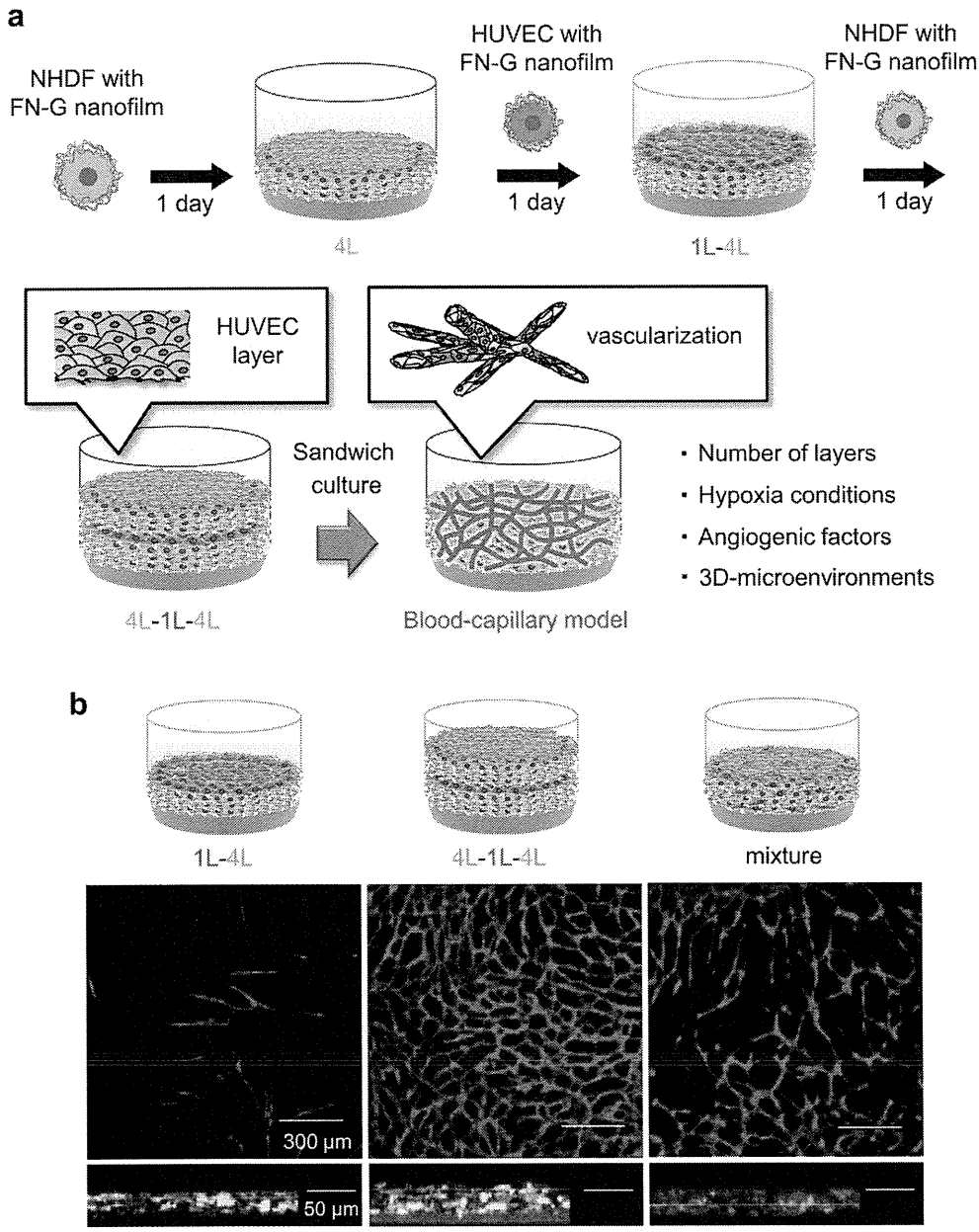

Fig. 1. In vitro vascularization by sandwich culture using the cell-accumulation technique. (a) Schematic illustration of the fabrication process of the endothelial tubule networks by the cell-accumulation technique. (b) CLSM cross-section images of 1L-4L tissue, 4L-1L-4L tissue, and a mixture of NHDFs and HUVECs after 7 days of incubation. The HUVECs were immunostained with an anti-CD31 antibody (red), and the NHDFs were labeled with CellTracker green (green).

secreted under hypoxic conditions, and 3D-microenvironments on the tubule formation of endothelial cells in vitro. Furthermore, the angiogenesis and lymphangiogenesis in human adipose-derived mesenchymal stem cell (MSC) tissues were also evaluated same as fibroblasts.

2. Materials & methods

2.1. Materials

All of the chemicals were used without further purification. Fibronectin (FN) from bovine plasma ($M_w = 4.6 \times 10^5$) and vascular endothelial growth factor (VEGF) were purchased from Sigma–Aldrich (MO, USA). Dulbecco's modified eagle medium (DMEM), gelatin (G) ($M_w = 1.0 \times 10^5$), tris(hydroxymethyl)aminomethane hydrochloride (Tris–HCl), 10% formalin solution, and 4% paraformaldehyde (PFA)/phosphate buffer solution were purchased from Wako Pure Chemical Industries (Osaka, Japan). ε-Lys ($M_w = 4700$) was kindly donated by CHISSO Corporation (Chiba, Japan). The monoclonal mouse anti-human CD31 antibody and the monoclonal mouse anti-collagen type IV were purchased from Dako (Glostrup, Denmark). Goat anti-mouse Alexa Fluor 488- and 546-conjugated IgG, 4′,6-diamidino-2-phenylindole dihydrochloride (DAPI), cell tracker green, Triton-X, fetal bovine serum (FBS), human adipose-derived mesenchymal stem cells (MSC), and MesenPRO RS medium were purchased from Life Technologies (CA, USA). The mouse anti-human VEGF antibody and the ELIZA assay kits for human VEGF, human hepatocyte growth factor (HGF) and human basic fibroblast growth factor (bFGF) were purchased from R&D systems (MN, USA). The cell culture insert with a 0.4 μm pore size was purchased from BD bioscience (NJ, USA) and Corning (NY, USA). Normal human dermal fibroblast (NHDF), human umbilical vein endothelial cell (HUVEC), human umbilical artery endothelial cell (HUAEC), human dermal lymphatic microvascular endothelial cell (LEC), and endothelial growth medium (EGM-2MV) were purchased from Lonza (NJ, USA). Mouse 10T1/2 and 3T3 cells were purchased from ATCC (VA, USA). The mouse pancreatic fibroblast cells (K643f) and mouse 3T3 fibroblast cells were kindly donated by Dr. M. R. Kano from Okayama University and Dr. K. Miyazono from Tokyo University.

2.2. Construction of the blood-capillary model by cell-accumulation technique

The NHDFs after trypsinization were suspended in 0.04 mg/ml of FN and G/Tris–HCl solution (50 mM, pH = 7.4), and alternately incubated for 1 min using a Micro-tube Rotator (MTR-103, AS ONE, Japan) with a washing step. The centrifugation was performed at 200× *g* for 1 min at each step. After 9 steps of coating, about 10 nm of the FN-G nanofilms were coated onto single cell surfaces. The cells were suspended in 0.3 ml of DMEM with 10% FBS, and were seeded onto 24 well trans-well inserts with a semipermeable membrane, and 1.4 ml of media was added into the micro-plates. After 1 h of incubation, another 1 ml of media was added to each well to connect the inner and outside media of the inserts, and the cells were then incubated in 5% CO_2 at 37 °C. After 1 day, NHDF tissues from a monolayer to 20 layers thickness were constructed. A 1×10^5 cells/layer aliquot was used for the 24 well inserts, and 2.5×10^5 cells/well for the 12 well inserts. In the same manner, 1×10^5 HUVEC cells were coated with FN-G nanofilms, and were seeded onto each NHDF tissue. The HUVECs adhered within 1 day to form a monolayer HUVEC-NHDF tissues. Moreover, the NHDFs coated with FN-G nanofilms accumulated on them, and thus a sandwich culture was performed. Normally, these cells were cultured for 1 week and fixed with a 4% PFA buffer solution for immunostaining. The NHDFs (passages: 4–10) were cultured in DMEM with 10% FBS. The HUVECs, HUAECs, and LECs (passages: 3–7) were cultured in EGM-2MV. The MSCs (passages: 3–7) were cultured in MesenPRO RS medium.

2.3. Immunofluorescent analysis

The NHDFs were stained with cell tracker green, and the endothelial cells were immunostained with an anti-CD31 antibody. Briefly, the tissues were permeabilized with 0.2% Triton-X for 15 min and blocked with 1% BSA/PBS for 1 h. The tissues were then incubated with the primary antibodies (1:50) for 1 h. After a washing step, the secondary antibodies (1:200) were added to the tissues. The tissues were finally observed by confocal laser scanning microscopy (CLSM, FLUOVIEW FV10i, Olympus, Japan) and confocal disk scan microscopy (DSU-IX81-SET, Olympus, Japan). For immunohistological observation of the blood-capillary models, an anti-Von Willebrand factor antibody was used. For measurements of the tubular lengths, cell numbers, branching points, mean lengths, and occupied area percentage, Metamorph software version 6.2r6 (Molecular Devices, USA) and WimTube (Wimasis, Germany) were used.

2.4. Oxygen partial pressure measurements

The oxygen partial pressure in the media was measured by an oxygen partial pressure meter (PO2-150S, Eikoukagaku, Tokyo, Japan). This device measured current value of oxygen on the surface of the electrode (POE-20W, Eikoukagaku, Tokyo, Japan) under a suitable voltage using the polarography principle to estimate oxygen partial pressure. The measurements were performed at a time point soon after seeding the NHDFs into the insert to form the 1L, 4L, 8L, and 4L-1L-4L tissues. The oxygen partial pressure of the medium without tissue was set as 150 mmHg. After 24 h, the media were changed, and the measurements were continued again.

2.5. Reverse transcription PCR analysis

The total RNA from the 1L, 4L, and 8L-NHDF tissues was extracted using an RNA micro scale kit (Life Technologies, CA, USA) according to the manufacturer's protocol. cDNA was prepared from 200 ng of total RNA using a cDNA synthesis kit. The reverse transcription polymerase chain reaction (RT-PCR) was performed with Taqman gene expression assays. The gene expression levels of the following targets were measured: VEGFA, HGF, bFGF, and glyceraldehyde 3-phosphate dehydrogenase (GAPDH). The relative quantification was performed by a comparative C_T method. The obtained gene expressions were normalized to GAPDH used as a house keeping gene.

2.6. ELISA measurement and the blocking test

VEGF, HGF, and bFGF from 1L-, 4L-, and 8L-tissues were measured by ELISA assay. A 2.3 ml aliquot of the supernatant from tissues in the 24 well inserts were collected, and added into a microplate from each ELISA assay kit. For the blocking tests, 4L-1L-4L tissues were exposed to media containing 100 ng of anti-VEGF antibody, and incubated for 1 week while changing the media every day. The tissues were then immunostained with anti-CD31 antibodies and observed by CLSM.

2.7. Fabrication of MSC tissue with blood- and lymph-capillary networks

4L-MSC tissues were constructed on 1L-HUVEC in the same manner as the NHDFs to obtain 4L-MSC-1L-HUVEC tissues after 3 days of incubation. To culture 4L-1L MSC tissues under hypoxic conditions, the medium in the insert was set at 0.3 ml, and the medium in the plate was set to 1.4 ml without connecting the medium between the insert and plate.

2.8. Statistical analysis

All data were expressed as means ± SD unless otherwise specified. For the PCR analysis, the values represent the mean ± SD from three independent experiments. Statistical comparisons between groups were analyzed by Student's *t*-test. Statistical differences from the PCR and ELISA analyses were determined by Tukey's multiple comparison test. A P value < 0.05 was considered to be statistically significant.

3. Results

3.1. Effect of the number of NHDF layers on tubular formation by sandwich culture

As shown by the CLSM observations from Fig. 1b, highly dense and homogeneous tubular networks were formed by a sandwich culture of HUVECs between 4L-NHDF tissues (4L-1L-4L) after 7 days in DMEM. On the other hand, tubular networks were not seen in the 1L-4L tissues, and almost all of the HUVECs disappeared after 7 days. Furthermore, in the case of a mixture of NHDFs and HUVECs, tubular structures were partially confirmed, but they were not homogeneous and did not connect with each other densely. These results suggest that a sandwich culture between NHDF multilayers would be the most suitable method to construct blood-capillary models. The density of the tubular networks could be controlled by adjusting the density of the sandwiched HUVECs (Fig. S1). Similarly, the components of the nanofilms on the cell surfaces affected the density of the tubular networks and FN and ε-Lys nanofilms containing cationic polymers reduced the tubular networks (Fig. S2). Furthermore, sandwiching HUAECs or LECs instead of HUVECs allowed them both to successfully form tubular networks in the whole tissue (Fig. S3) [24]. To investigate the relationship between the number of NHDF layers and the formation of tubular structures, structural observation of the HUVECs sandwiched between the different numbers of NHDF layers was performed by CLSM (Fig. 2 and Fig. S4). Each tissue was constructed by a sandwich culture of HUVECs between 1L- and 10L-NHDF layers. As a result, more than 3 layers of NHDF tissues induced morphological change in the HUVECs to form tubular networks (Fig. 2a). A quantitative analysis of the tubular structures showed that the total tubular length and number increased upon increasing the number of sandwiching NHDF layers, especially with more than 4L-tissues (Fig. 2b, c). Many branching points of the tubular structures were also seen in sandwich culture using thick NHDF tissues, and the mean tubular lengths estimated from the tubular length between the branching points were almost the same in all samples (Fig. 2d, e).

3.2. Structural observations of HUVEC networks

We performed immunohistochemistry with an anti-Von Willebrand factor antibody (Fig. 3a, b). There were many lumenal structures distributed three-dimensionally in the tissues, and the area of the HUVECs and lumen increased upon increasing the number of NHDF layers, as well as the tubular length and number in Fig. 2 (Fig. S5). Type IV collagen, which is one of the components of the basement membrane, was strongly expressed around the lumens of the HUVEC (Fig. 3c, d). Through the deposition of the perivascular ECM (black arrow) and the formation of the endoplasmic reticulum (red arrow), the appropriate apical-basal polarity of the HUVECs was confirmed. The perivascular ECM with positive staining of collagen type IV would be secreted from NHDFs and HUVECs during the sandwich culture. We confirmed the structures of the ECM and the formation of adherens junctions by transmission electron microscopy (TEM) observations (Fig. 3e, f). The HUVECs attached tightly with each other, and formed lumenal structures which were stabilized through adherens junctions as well as blood vessels in the living body.

3.3. Measurements of hypoxic conditions and angiogenic factors

To measure hypoxia in the 3D-microenvironment, the oxygen partial pressure in the media was measured during incubation (Fig. 4a). As a result, the oxygen partial pressure of the 8L and 4L-1L-4L tissues decreased rapidly to half of the starting value within

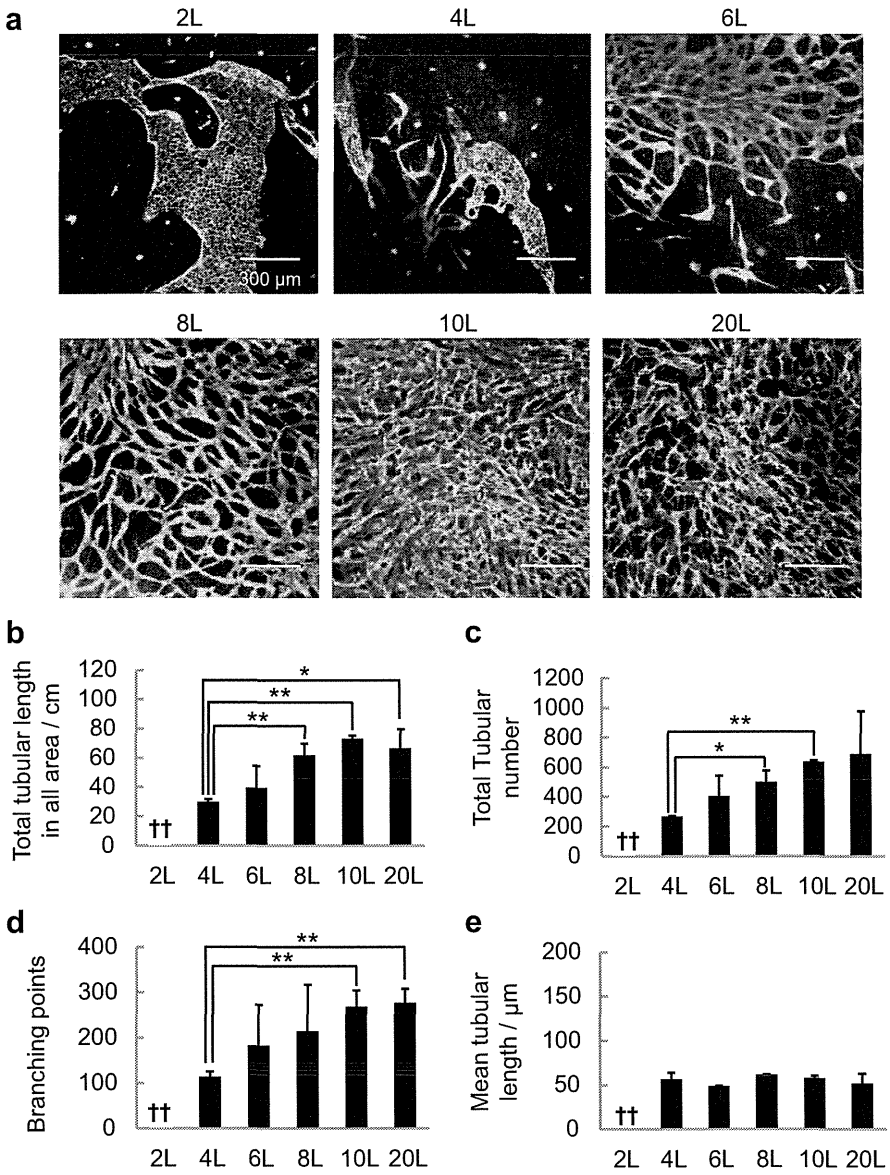

Fig. 2. Effect of the number of NHDF layers on tubule formation. (a) CLSM images of blood-capillary models constructed by a sandwich culture of HUVECs between 1L- and 10L-NHDF tissues for 7 days. (b–e) Quantification of the total tubule length in all areas, the total tubule number, the number of branching points, and the mean tubule length of the HUVEC networks ($n = 3$). ††: Tubular networks were not confirmed in 2L-tissues. *$P < 0.05$, **$P < 0.01$ when compared with 4L.

several hours. Once the oxygen partial pressures returned to their original values by changing the media after 24 h, it decreased again within 3 h. To check the gene expression of angiogenic factors such as VEGFA, HGF and basic fibroblast growth factor under hypoxic conditions, real time RT-PCR measurements were performed (Fig. 4b). The gene expression of VEGF and HGF in 4L-tissues were 1.5–2-fold higher than that of 1L-tissues after 24 h of incubation, whereas the gene expression of bFGF decreased upon increasing the number of NHDF layers. Three types of angiogenic factors secreted from each tissue after 24 h were measured by ELISA assays. The secretion of VEGF, HGF, and bFGF drastically increased upon increasing the number of NHDF layers (Fig. 4c–e). In particular, the 8L-tissue secretion of VEGF, which is one of the most important factors for angiogenesis through the activation of migration, proliferation, and differentiation of endothelial cells, showed a more than 60-fold increase as compared to 1L-tissues. To confirm the effect of VEGF on tubule formation, an anti-VEGF antibody was used as a blocking experiment. We exposed the blood-capillary models to the media containing 100 ng of anti-VEGF antibody per sample. This value is equivalent to 10 times as much as VEGF secreted from 8L-NHDF tissues estimated form ELISA result in Fig. 4c. As a result, the HUVECs did not form very dense and homogeneous tubular structures by inhibiting the functions of VEGF, thus indicating that angiogenic factors played important roles in tubule formation (Fig. 4f, g). Furthermore, to understand the effects of long-term culture on angiogenesis, the gene expression of angiogenic factors in 1L-, 5 L-, 10L-, and 20L-NHDF tissues after 2, 7, 10, and 14 days of incubation were analyzed by RT-PCR measurements (Fig. 5 and Fig. S6). Comparing the gene expressions of the NHDF multilayers versus NHDF monolayers, all gene expressions showed drastic increases (up to a 40-fold increase) in contrast with the gene expression of NHDF tissues after 1 day of incubation. The gene expressions increased with increasing layer number, and these high gene expression levels were maintained even after 14 days of incubation.

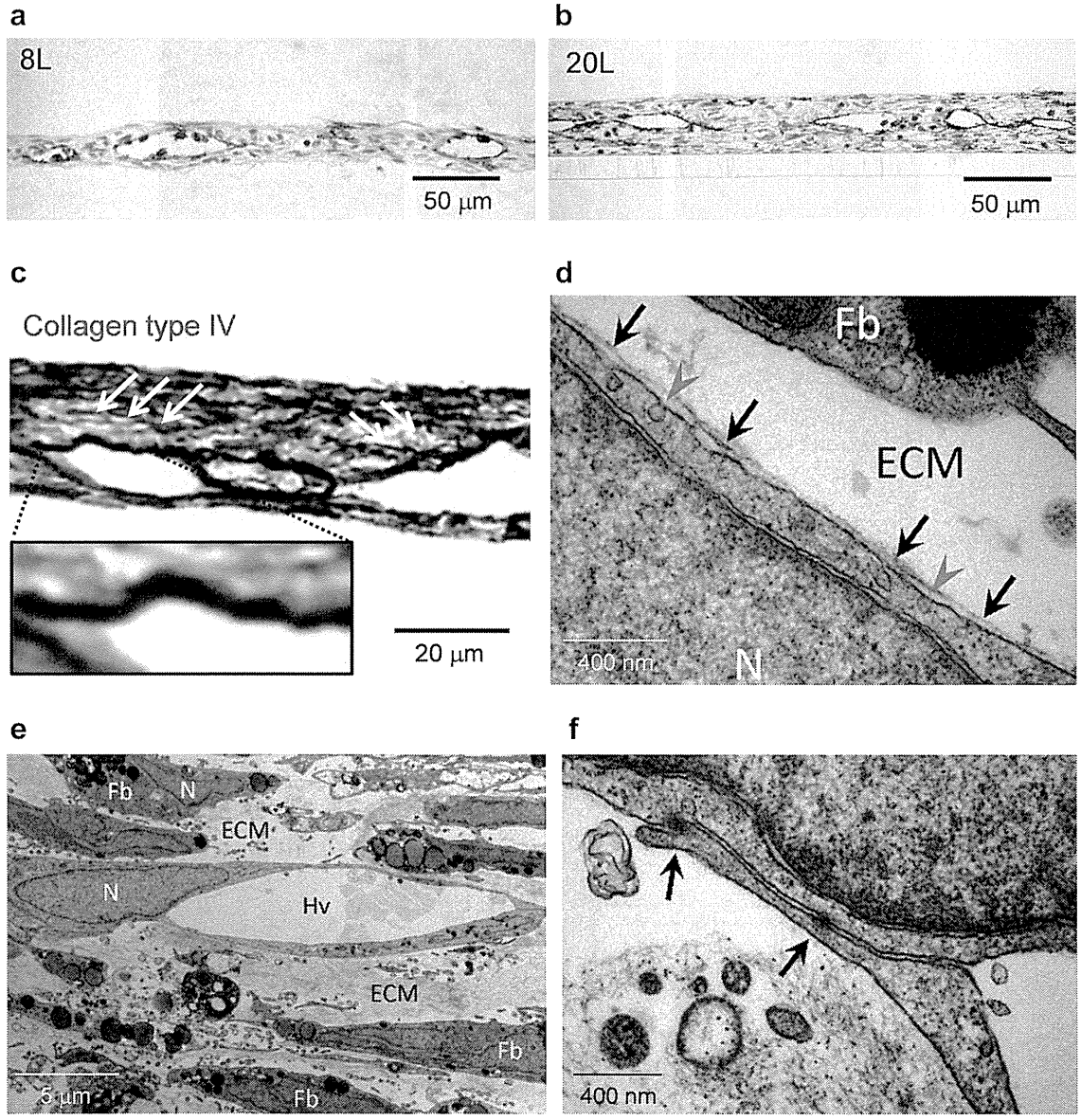

Fig. 3. Immunohistological and TEM observations. Immunohistological images of (a) 4L-1L-4L and (b) 10L-1L-10L tissues immunostained with an anti-Von Willebrand factor antibody. Structural analysis by (c) immunohistological and (d) TEM observations of basement membranes and (e, f) TEM observations of adherens junctions in 10L-1L-10L tissues. An anti-collagen type IV antibody was used for the immunostaining experiments. The black arrows denote the deposition of ECM and the red arrows show the formation of the endoplasmic reticulum. N: nucleus, Fb: fibroblast, Hv: lumen of HUVEC. (For interpretation of the references to color in this figure legend, the reader is referred to the web version of this article.)

3.4. *Effect of 3D-microenvironments on tubular formation*

To understand whether the 3D-microenvironment around the HUVECs is essential for tubule formation, the HUVEC monolayers were cultured under various conditions (Fig. 6a). Even though the HUVEC monolayers were exposed to media containing a sufficient amount of VEGF (10 ng) or collected from NHDF multilayers that secreted angiogenesis factors, there were no morphological changes, and the HUVECs maintained their cobble stone structures after 5 days. Next, we tried to investigate what microenvironment could induce tubular formation in detail. To do this, 1L-4L, 2L-1L-2L, and 4L-1L tissues were constructed, and their HUVEC structures were observed. To evaluate the effects of only the 3D-microenvironment, the total number of NHDF layers was standardized to 4 layers, which means that the same amount of angiogenic factors was in each sample, although the local position of NHDFs was different in each tissue. The HUVECs were put at the top (1L-4L), middle (2L-1L-2L), and bottom (4L-1L) of 4L-tissues (Fig. 6b, c). As a result, only the 4L-1L tissues induced tubular formation of the HUVECs, even though the total number of NHDF layers was less than 4 layers.

3.5. *Fabrication of multilayered MSC tissues with blood- and lymph-capillary networks*

Finally, we fabricated MSC vasculogenesis models based on knowledge obtained from the introduction of blood capillaries into fibroblast tissues. Since the angiogenic factors secreted from the surrounding tissues under hypoxic conditions and the 3D-microenvironments above the HUVECs play important roles in vascularization (Fig. 7a), we exposed the 4L-MSC-1L-HUVEC tissues to hypoxic conditions, which satisfied above requirements. To induce

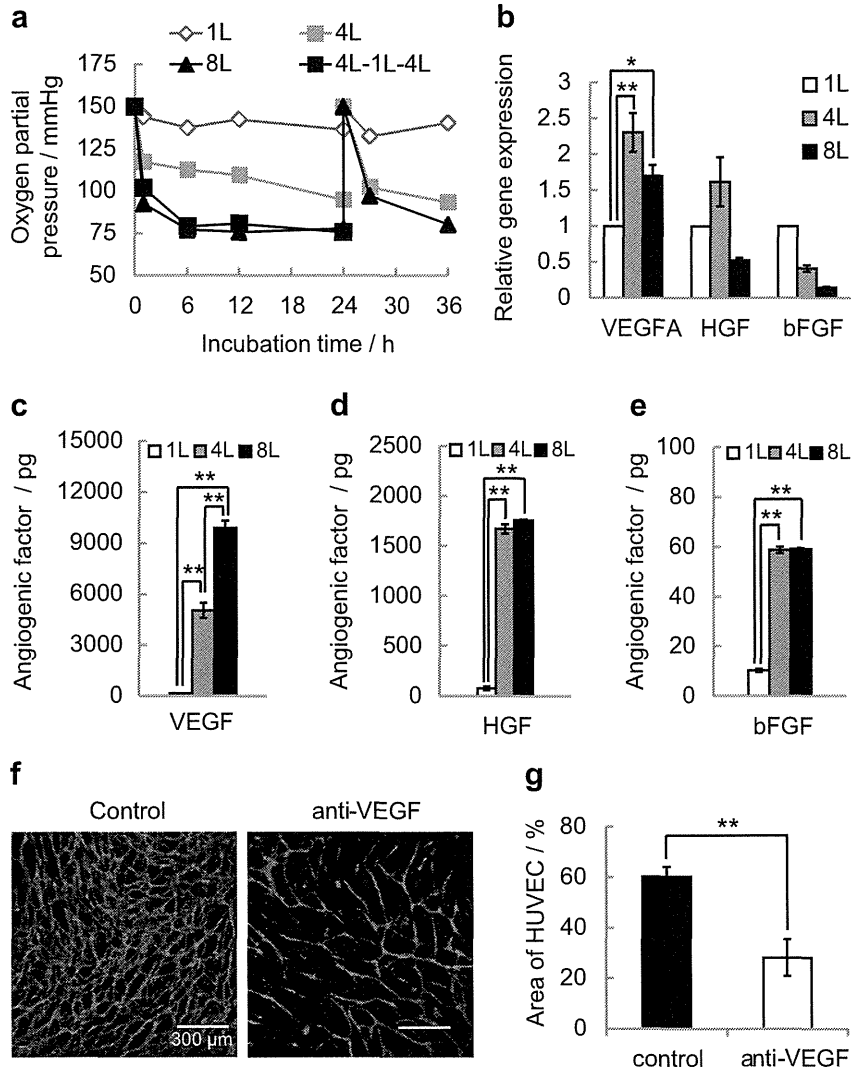

Fig. 4. Gene expression and secretion of angiogenic factors under hypoxic conditions. (a) Measurements of the oxygen partial pressure in the media of 1L, 4L, 8L, and 4L-1L-4L tissues. (b) Relative gene expression and (c–e) ELISA analysis of the VEGFA, HGF, and bFGF levels of 1L-, 4L-, and 8L-NHDF tissues after 24 h of incubation ($n = 3$). The transcripts were normalized to GAPDH. (f) CLSM images and (g) the area of the tubule networks in 10L-1L-10L tissues cultured without and with an anti-VEGF antibody ($n = 3$). $^{*}P < 0.05$, $^{**}P < 0.01$ when compared with 1L, 4L, or control (Tukey's multiple comparison test).

the hypoxic conditions, MSC tissue was cultured in a lower volume of media as compared to the control. As a result, the oxygen partial pressure of the 4L-MSC tissues in the lower volume of culture media decreased significantly during the initial 3 h of incubation (Fig. 7b). Next, we constructed 4 types of MSC tissues (1L-1L, 4L-1L, 4L-1L cultured under hypoxia, and 4L-1L cultured in VEGF-containing media) and checked the degree of vascularization of the HUVECs after 3 days of incubation by anti-CD31 antibody immunostaining. HUVECs in 1L-1L tissue did not form tubular structures, as well as the NHDF tissue. Although the 4L-1L tissues formed HUVEC tubular networks, there were many discontinuous structures and defects (Fig. 7c). On the other hand, the 4L-1L tissues under hypoxia have more continuous and homogeneous tubular networks and the area of the HUVEC networks was greater than the 4L-1L tissue, suggesting that the hypoxic conditions promoted tubular formation in the MSC tissue (Fig. 7c, d). There were no significant differences between the 4L-1L as a control and 4L-1L in VEGF-containing media, even though angiogenic factors were added to the media.

Furthermore, this vascularization method was applied to the fabrication of a lymph-capillary model of MSCs. In the same manner as HUVEC tubular formation, the 4L-MSC-1L-LEC tissue was constructed. As shown in the fluorescent image of the 4L-MSC-1L-LEC tissue immunostained with an anti-CD31 antibody in Supplementary Fig. S9a, lymphatic tubular structures were successfully formed and they had clear lumenal images after 3 days of incubation. Amazingly, when HUVECs and LECs were introduced into the MSC tissue at the same time and at the same plane, the HUVEC and LEC tubular networks were formed separately in the MSC tissue (Fig. S9b), which are in agreement with the results of the NHDF sandwich culture [24].

4. Discussion

We have reported a bottom-up approach to construct 3D-vascularized tissues by the cell-accumulation technique using ECM nanofilms on single cell surfaces [18]. During tubule formation, the HUVECs spontaneously assembled and could form networks by adjusting the culture conditions such as the 3D-microenvironment, hypoxia conditions, and angiogenic factors, as well as the angiogenesis process in the body. TEM images clearly revealed the adherens junctions between HUVECs in the networks. Interestingly,

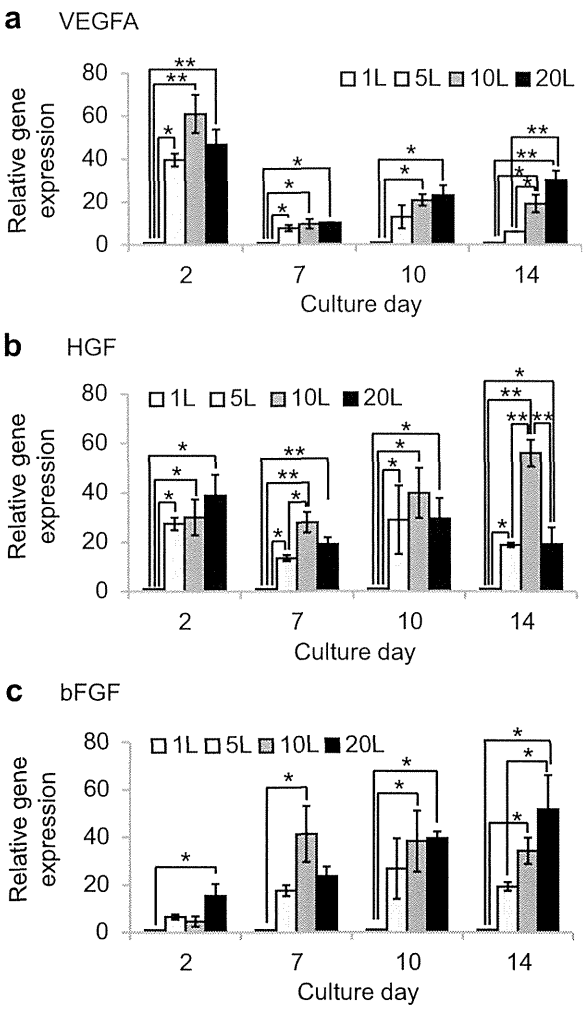

Fig. 5. Effect of long-term culture on angiogenic factor expression. The relative gene expression of (a) VEGFA, (b) HGF, and (c) bFGF of the NHDF multilayers after 2, 7, 10, and 14 days of incubation ($n = 3$). The transcripts were normalized to GAPDH. $^{*}P < 0.05$, $^{**}P < 0.01$ (Tukey's multiple comparison test).

we recently found HUVECs formed the developed adherens junctions, while LEC displayed irregular shape, loose adhesive connection and gap formation [24], suggesting FN-G nanofilms with mesh-work fiber structures [25] did not inhibit the formation of adherens junctions to recreate the junction structures of blood and lymph vessels in vivo. As shown in Fig. 2, we found that a sandwich culture of HUVECs of more than 3L-NHDF tissues was required for tubule formation. We focused on the roles of angiogenic factors to promote angiogenesis. Angiogenic factors such as VEGFA, HGF, and bFGF are secreted from surrounding tissues that lack nutrients and oxygen under hypoxic conditions [26]. Since these angiogenic factors are known to activate the functions of endothelial cells to induce migration, proliferation, and differentiation, they have been widely employed by fixation in hydrogels to achieve in vitro vascularization. As shown in Figs. 4 and 5, the increase in the number of NHDF layers resulted in an increase in angiogenic factor secretion through the decreased oxygen concentration, suggesting that angiogenic factors secreted from the NHDF multilayers caused tubule formation through the activation of HUVECs. Therefore, we assumed that the total amount of angiogenic factors would be important for in vitro vascularization. Actually, all of the angiogenic factors measured in this study were secreted at much higher concentrations from the NHDF multilayers than from the NHDF monolayer, and the blocking experiments showed the importance of VEGFA for tubule formation (Fig. 4d–e). The reason why the 3D-engineered tissues produced a greater amount of angiogenic factors is believed to be various 3D-effects such as central hypoxia, 3D-cell adhesion, and stiffness, indicating that this 3D-technology can mimic the angiogenesis process in a living body [27–29].

Although the secretion of angiogenic factors plays a crucial role in tubule formation, when the HUVEC monolayers were exposed to media containing VEGF or collected from NHDF multilayers cultured separately, they did not change their morphologies in spite of the adequate angiogenic factors (Fig. 6a). These results revealed that not only angiogenic factors, but also 3D-microenvironments, are essential to start tubule formation. To confirm the requirements for tubule formation in detail, we observed the structures of HUVECs arranged in the top, middle, and bottom of 4L-NHDF tissues. Only the 4L-1L tissues formed tubular structures, even though the amount of angiogenic factors was almost the same as the 1L-4L and 2L-1L-2L tissues, indicating that the microenvironments above the HUVECs determined whether in vitro vascularization occurs. These results can be understood by the vertical migration and assembly of HUVECs in the NHDF tissues. Sandwiched between the 2L-NHDF layers, the HUVECs migrated to the top of the tissues and then detached from tissue because we used DMEM without any cytokines. On the other hand, the arrangement of the greater than 4L-NHDF tissues above the HUVECs led to tubule formation, which is believed to be related to the distance from the HUVEC to the top of the NHDF tissues. Kino-oka and co-workers reported that HUVEC network formation depends on the HUVECs encountering and making connections when 5L myoblast sheets were placed on various densities of HUVEC monolayer [30]. Therefore, HUVEC assembly occurred effectively as compared to vertical migration when the arranged thick NHDF tissues on the HUVEC monolayer formed high density tubular networks. Currently, there are some reports on the construction of vascularized tissues by 3D-culture in scaffolds where various cytokines were fixed, co-cultured with pericytes, and cell sheet engineering. However, the detailed requirements of in vitro vascularization are still unclear, because these methods have limitations in controlling the 3D-microenvironments of the cells at the single layer level. Since this cell-accumulation technique is able to control the 3D-culture conditions at the single layer level without complicated procedures, this method would be useful to recreate 3D-microenvironments for in vitro vascularization, and to investigate the mechanisms of tubule formation.

Furthermore, when applying these results to MSC tissues, the vascularized MSC tissues were successfully fabricated in vitro. Comparing to NHDFs, MSC tissues might require higher hypoxic condition media because the section of angiogenic factors significantly depends on cell type. Both the 3D-microenvironments above the HUVECs and the hypoxic conditions that can induce angiogenic factor secretion from MSCs contributed to the formation of blood- and lymph-capillary networks in the MSC tissues. To the best of our knowledge, this is the first example of the fabrication of MSC tissues with blood- and lymph-capillary networks. This knowledge can be used for the vascularization of other tissues, such as the liver and pancreas [31]. On the other hand, the cell types and their derivation strongly influenced the cell behaviors and cell–cell interactions. For example, human pancreatic fibroblast cells (K643f) and mouse 3T3 fibroblast cells did not induce HUVEC tubule formation during sandwich culture (Fig. S7). Therefore, the appropriate 3D-microenvironment for endothelial cells should be prepared to introduce blood capillaries into other tissues. These in vitro blood-capillary models have potential as angiogenesis assays, especially for tumor angiogenesis assays which for cancer

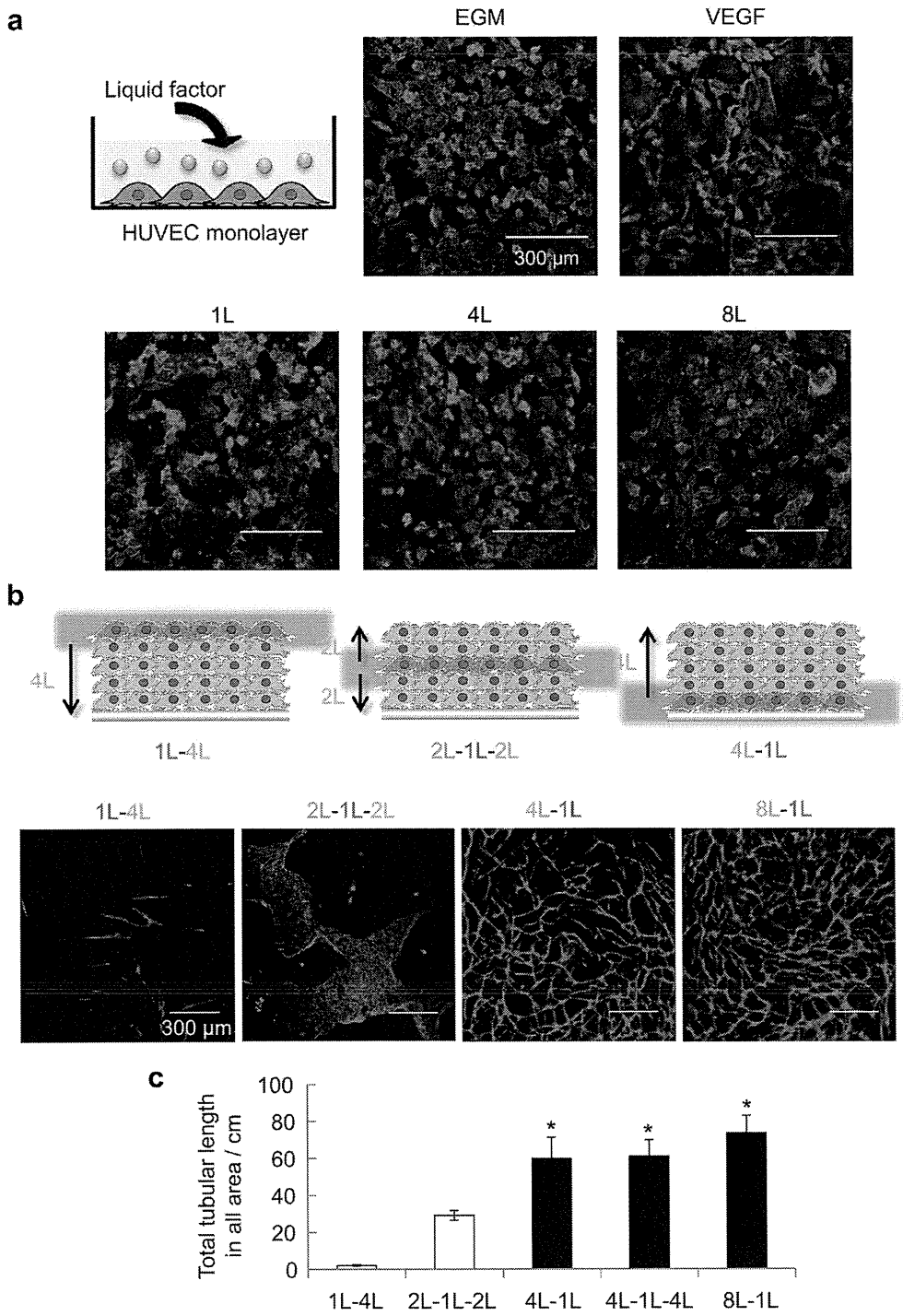

Fig. 6. Effect of the 3D-microenvironment. (a) Fluorescent microscopic images of HUVEC monolayers exposed to media containing VEGF or collected from 1L-, 4L-, and 8L-NHDF tissues for 5 days. (b) CLSM images and (c) the total tubule length of each tissue after 7 days of incubation ($n = 3$). The HUVECs were immunostained with an anti-CD31 antibody (red). *$P < 0.05$ when compared with 1L-4L (Tukey's multiple comparison test).

therapy, and allow enable the evaluation of the potential effects of drugs and drug carriers in vitro [32–34].

5. Conclusions

In summary, we investigated the effects of 3D-microenvironments and angiogenic factors on in vitro vascularization by sandwich culture using the cell-accumulation technique. By increasing the NHDF layer number, the gene expression and angiogenic factor secretion of the NHDF multilayers under hypoxic conditions increased, as compared to NHDF monolayers, to promote tubule formation of the HUVECs. We found that the 3D-microenvironments around the HUVECs, especially above the HUVECs, were important for tubule formation because more than 4L-NHDF tissues generated tubular networks, but less than 2L-NHDF tissues did not. Furthermore, the introduction of blood- and lymph-capillary

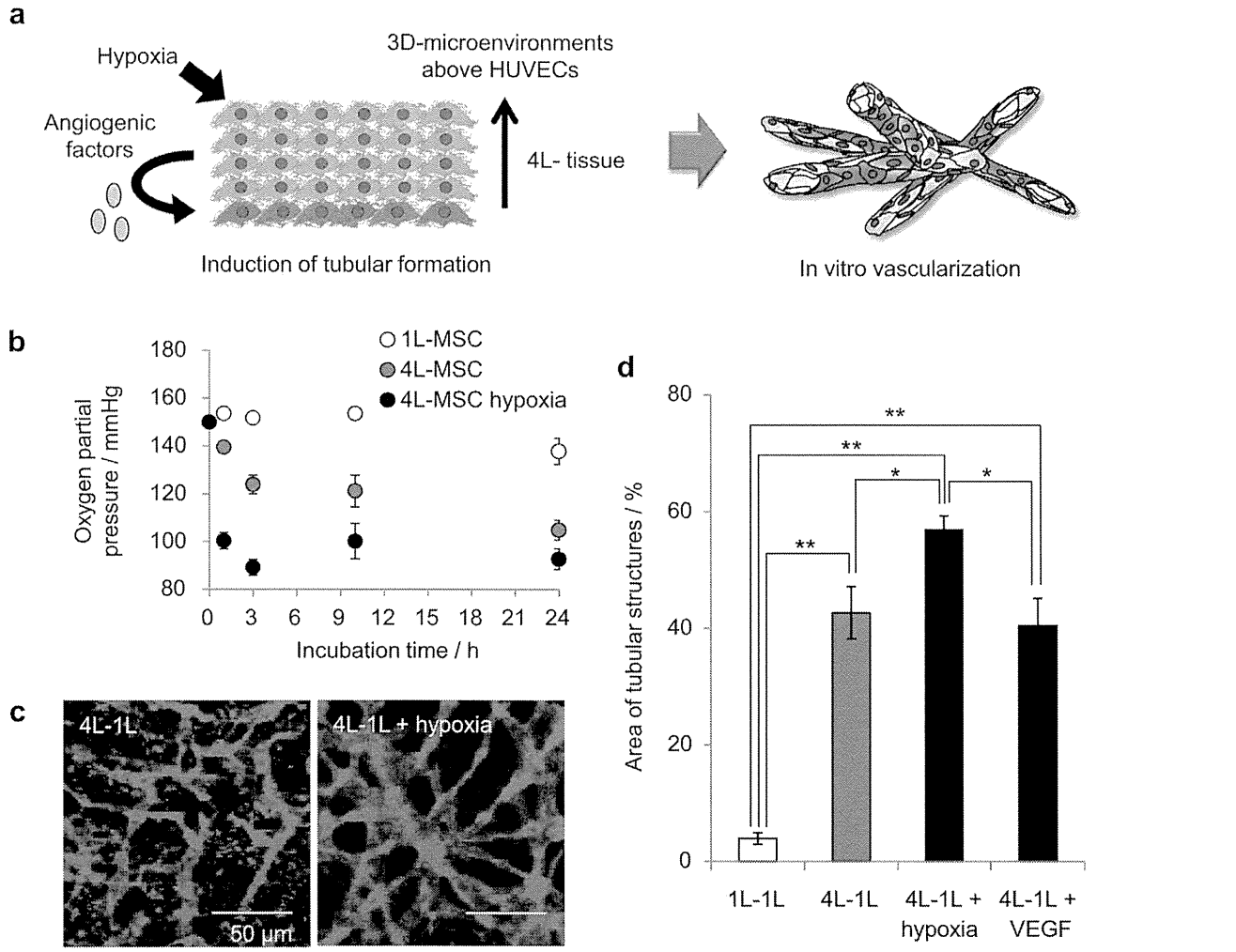

Fig. 7. MSC tissues with blood- and lymph-capillary networks. (a) Oxygen partial pressure of 1L-, 4L-, and 4L-MSC tissues under hypoxia during 36 h of incubation ($n = 3$). (b) CLSM images and (c) the area of the tubule structures of each MSC tissue after 3 days of incubation ($n = 3$). $^{*}P < 0.05$, $^{**}P < 0.01$ (Tukey's multiple comparison test).

networks into the MSC tissues was also achieved by altering the 3D-microenvironments for the first time. These findings would be useful for tissue engineering that needs the introduction of blood vessels, and for investigations into biological mechanisms such as tumor angiogenesis.

Acknowledgments

This work was supported by the NEXT Program (LR026), a Grant-in-Aid for Scientific Research (S), and the SENTAN-JST Program. We also thank Akiko Seo for her technical assistance.

Appendix A. Supplementary data

Supplementary data related to this article can be found at http://dx.doi.org/10.1016/j.biomaterials.2014.01.079.

References

[1] Isenberg BC, Wong JY. Building structure into engineered tissues. Mater Today 2006;9:54–60.
[2] Radisic M, Yang L, Boublik J, Cohen RJ, Langer R, Freed LE, et al. Medium perfusion enables engineering of compact and contractile cardiac tissue. Am J Physiol Heart Circ Physiol 2004;286:507–16.
[3] Lammert E, Cleaver O, Melton D. Induction of pancreatic differentiation by signals from blood vessels. Science 2001;294:564–7.
[4] Folkman J, Haudenschild C. Angiogenesis in vitro. Nature 1980;288:551–6.
[5] Madri JA, Williams SK, Wyatt T, Mezzio C. Capillary endothelial cell cultures: phenotypic modulation by matrix components. J Cell Biol 1983;97:153–65.
[6] Chiu LLY, Radisic M. Scaffolds with covalently immobilized VEGF and angiopoietin-1 for vascularization of engineered tissues. Biomaterials 2010;31:226–41.
[7] Moon JJ, Saik JE, Poché RA, Leslie-Barbick JE, Lee SH, Smith AA, et al. Biomimetic hydrogels with pro-angiogenic properties. Biomaterials 2010;31:3840–7.
[8] Levenberg S, Rouwkema J, Macdonald M, Garfein ES, Kohane DS, Darland DC, et al. Engineering vascularized skeletal muscle tissue. Nat Biotechnol 2005;23:879–84.
[9] Armulik A, Genové G, Betsholtz C. Pericytes: developmental, physiological, and pathological perspectives, problems, and promises. Dev Cell 2011;21:193–215.
[10] Koike N, Fukumura D, Gralla O, Au P, Schechner JS, Lain RK. Creation of long-lasting blood vessels. Nature 2004;428:138–9.
[11] Grainger SJ, Putnam AJ. Assessing the permeability of engineered capillary networks in a 3D culture. PLoS One 2011;6:e22086.
[12] Sasagawa T, Shimizu T, Sekiya S, Haraguchi Y, Yamato M, Sawa Y, et al. Design of prevascularized three-dimensional cell-dense tissues using a cell sheet stacking manipulation technology. Biomaterials 2010;31:1646–54.
[13] Asakawa N, Shimizu T, Tsuda Y, Sekiya S, Sasagawa T, Yamato M, et al. Pre-vascularization of in vitro three-dimensional tissues created by cell sheet engineering. Biomaterials 2010;31:3903–9.
[14] Haraguchi Y, Shimizu T, Sasagawa T, Sekine H, Sakaguchi K, Kikuchi T, et al. Fabrication of functional three-dimensional tissues by stacking cell sheets in vitro. Nat Protoc 2012;7:850–8.
[15] Miller JS, Stevens KR, Yang MT, Baker BM, Nguyen DHT, Cohen DM, et al. Rapid casting of patterned vascular networks for perfusable engineered three-dimensional tissues. Nat Mater 2012;11:768–74.

[16] Zheng Y, Chen J, Craven M, Choi NW, Totorica S, Diaz-Santana A, et al. In vitro microvessels for the study of angiogenesis and thrombosis. Proc Natl Acad Sci U S A 2012;109:9342–7.
[17] Yoshida H, Matsusaki M, Akashi M. Multilayered blood capillary analogs in biodegradable hydrogels for in vitro drug permeability assays. Adv Funct Mater 2013;23:1736–42.
[18] Nishiguchi A, Yoshida H, Matsusaki M, Akashi M. Rapid construction of three-dimensional multilayered tissues with endothelial tube networks by the cell-accumulation technique. Adv Mater 2011;23:3506–10.
[19] Matsusaki M, Kadowaki K, Nakahara Y, Akashi M. Fabrication of cellular multilayers with nanometer-sized extracellular matrix films. Angew Chem Int Ed 2007;46:4689–92.
[20] Matsusaki M, Ajiro H, Kida T, Serizawa T, Akashi M. LbL assembly through weak interactions and their biomedical applications. Adv Mater 2012;24:454–74.
[21] Matsusaki M, Kadowaki K, Adachi E, Sakura T, Yokoyama U, Ishikawa Y, et al. Morphological and histological evaluations of 3D-layerd blood vessel constructs prepared by hierarchical cell manipulation. J Biomater Sci Polym Ed 2012;23:63–79.
[22] Matsusaki M, Sakaue K, Kadowaki K, Akashi M. Three-dimensional human tissue chips fabricated by rapid and automatic inkjet cell printing. Adv Healthcare Mater 2013;2:534–9.
[23] Sasaki J, Matsumoto T, Egusa H, Matsusaki M, Nishiguchi A, Nakano T, et al. In vitro reproduction of endochondral ossification using a 3D mesenchymal stem cell construct. Integr Biol 2012;4:1207–14.
[24] Asano Y, Nishiguchi A, Matsusaki M, Okano D, Saito E, Akashi M, et al. Ultrastructure of blood and lymphatic vascular networks in three-dimensional cultured tissues fabricated by ECM nanofilm-based cell accumulation technique. Microscopy, Ms: MICRO-2013-00063.R1.
[25] Kadowaki K, Matsusaki M, Akashi M. Control of cell surface and functions by layer-by-layer nanofilms. Langmuir 2010;26:5670–8.
[26] Harris AL. Hypoxia – a key regulatory factor in tumor growth. Nat Rev Cancer 2002;2:38–47.
[27] Cukierman E, Pankov R, Stevens DR, Yamada KM. Taking cell-matrix adhesions to the third dimension. Science 2001;294:1708–12.
[28] Discher DE, Janmey P, Wang Y. Tissue cells feel and respond to the stiffness of their substrate. Science 2005;310:1139–43.
[29] Fischbach C, Chen R, Matsumoto T, Schmelzle T, Brugge JS, Polverini PJ, et al. Engineering tumors with 3D scaffolds. Nat Methods 2007;4:855–60.
[30] Nagamori E, Ngo TX, Takezawa Y, Saito A, Sawa Y, Shimizu T, et al. Network formation through active migration of human vascular endothelial cells in a multilayered skeletal myoblast sheet. Biomaterials 2013;34:662–8.
[31] Kaufman-Francis K, Koffler J, Weinberg N, Dor Y, Levenberg S. Engineered vascular beds provide key signals to pancreatic hormone-producing cells. PLoS One 2012;7:e40741.
[32] Bergers G, Benjamin LE. Tumorigenesis and the angiogenic switch. Nat Rev Cancer 2003;3:401–10.
[33] Smalley KSM, Lioni M, Noma K, Haass NK, Herlyn M. In vitro three-dimensional tumor microenvironment models for anticancer drug discovery. Expert Opin Drug Discovery 2008;3:1–10.
[34] Peer D, Karp JM, Hong S, Farokhzad OC, Margalit R, Langer R. Nanocarriers as an emerging platform for cancer therapy. Nat Nanotechnol 2007;2:751–60.

J Bone Miner Metab
DOI 10.1007/s00774-013-0547-5

SHORT COMMUNICATION

Development of an in vitro culture method for stepwise differentiation of mouse embryonic stem cells and induced pluripotent stem cells into mature osteoclasts

Keizo Nishikawa · Yoriko Iwamoto · Masaru Ishii

Received: 6 August 2013 / Accepted: 7 November 2013

Abstract The development of methods for differentiation of embryonic stem cells (ESCs) and induced pluripotent stem cell (iPSCs) into functional cells have helped to analyze the mechanism regulating cellular processes and to explore cell-based assays for drug discovery. Although several reports have demonstrated methods for differentiation of mouse ESCs into osteoclast-like cells, it remains unclear whether these methods are applicable for differentiation of iPSCs to osteoclasts. In this study, we developed a simple method for stepwise differentiation of mouse ESCs and iPSCs into bone-resorbing osteoclasts based upon a monoculture approach consisting of three steps. First, based on conventional hanging-drop methods, embryoid bodies (EBs) were produced from mouse ESCs or iPSCs. Second, EBs were cultured in medium supplemented with macrophage colony-stimulating factor (M-CSF), and differentiated to osteoclast precursors, which expressed CD11b. Finally, ESC- or iPSC-derived osteoclast precursors stimulated with receptor activator of nuclear factor-B ligand (RANKL) and M-CSF formed large multinucleated osteoclast-like cells that expressed tartrate-resistant acid phosphatase and were capable of bone resorption. Molecular analysis showed that the expression of osteoclast marker genes such as *Nfatc1*, *Ctsk*, and *Acp5* are increased in a RANKL-dependent manner. Thus, our procedure is simple and easy and would be helpful for stem cell-based bone research.

Keywords Induced pluripotent stem cell · Embryonic stem cell · Osteoclast · Differentiation · Bone resorption

K. Nishikawa (✉) · Y. Iwamoto · M. Ishii
Department of Immunology and Cell Biology, Graduate School of Medicine/Frontier Biosciences, Osaka University, Yamada-oka 2-2, Suita, Osaka 565-0871, Japan
e-mail: nishi@ifrec.osaka-u.ac.jp

K. Nishikawa · M. Ishii
WPI-Immunology Frontier Research Center, Osaka University, Yamada-oka 2-2, Suita, Osaka 565-0871, Japan

Y. Iwamoto
Department of Otolaryngology Head and Neck Surgery, Osaka University, Yamada-oka 2-2, Suita, Osaka 565-0871, Japan

M. Ishii
Japan Science and Technology Agency, CREST, 5 Sanban-cho, Chiyoda-ku, Tokyo 102-0075, Japan

Introduction

The maintenance of bone homeostasis is dependent on the balance between bone-resorbing osteoclasts and bone-forming osteoblasts [7, 8]. Excessive bone resorption by osteoclasts is often associated with diseases accompanied by pathological bone loss, including osteoporosis and rheumatoid arthritis [9–12]. Bisphosphonates are potent inhibitors of osteoclast-mediated bone resorption and are effective antiresorptive drugs for the treatment with osteoporosis. However, reports of osteonecrosis of the jaw have emerged with long-term use of bisphosphonates [13]. In addition, questions have also emerged regarding the association between bisphosphonates and other rare adverse events such as esophageal cancer [14], raising questions regarding their long-term safety. Therefore, further development of antiresorptive drugs is required to minimize its occurrence. Because high-throughput screening (HTS) in cell-based assays is very often used to identify lead compounds for a wide range of therapeutic areas, an HTS-suitable osteoclast differentiation protocol is required.

Published online: 24 December 2013

The potency of embryonic stem cells (ESCs) and induced pluripotent stem cells (iPSCs) to undergo unlimited self-renewal and extensive differentiation makes them an attractive source for cell-based assays for disease modeling, drug discovery, and regeneration therapies [1, 2]. Although there are several reports on in vitro osteoclast differentiation of mouse ESCs [3–6], most of these methods are laborious because of the required use of OP9 coculture. Furthermore, it is unclear whether these methods are applicable for differentiation of mouse iPSCs to osteoclasts. In this article, we report a simple method for stepwise differentiation of mouse ESCs and iPSCs into bone-resorbing osteoclasts based upon a monoculture approach. Our procedure would be helpful for antiresorptive discovery as well as cell-based bone research.

Materials and methods

Cell culture

Mouse ESCs (J1 line) [15] and iPSCs (38c2 and 20D17 lines) [16] were cultured under self-renewal conditions on mitomycin C-inactivated mouse embryo fibroblasts (Millipore) in standard ES media [Knockout DMEM (Gibco), supplemented with 15 % fetal bovine serum (FBS) (Hyclone), 1× nonessential amino acids, 2 mM L-glutamine, 100 U/ml penicillin, 100 mg/ml streptomycin, 0.1 mM β2-mercaptoethanol (all from Gibco), and with 1,000 U/ml leukemia inhibitory factor (LIF) (Wako)].

For embryoid body (EB) formation, mouse ESCs and iPSCs on mouse embryo fibroblasts (MEFs) were trypsinized, and MEF layers were separated from ESCs and iPSCs cells by culturing at 37 °C for 30 min. Nonadherent cells, which contain undifferentiated ESCs and iPSCs, were resuspended in EB medium [Iscove's modified Dulbecco's medium (IMDM; Invitrogen), 2 mM L-glutamine (Wako), penicillin/streptomycin (Invitrogen), 5 % PFHM-II (Invitrogen), 50 μg/ml ascorbic acid (Nacalai), 200 μg/ml iron-saturated holo-transferrin (Sigma), 450 μM monothioglycerol (Sigma), and 15 % ES cell hematopoietic differentiation FBS (StemCell Technologies)]. To prepare hanging drops, 25 μl/drop cell suspension (3,000 cells) was pipetted onto the inner portion of a tissue culture plate lid. Hanging drops were cultured for 2 days at 37 °C in 5 % CO_2.

For differentiation, 20–50 EBs were transferred into one well of a six-well plate containing 4 ml culture medium [minimum essential media-alpha (alphaMEM; Invitrogen), 10 % fetal calf serum and penicillin/streptomycin (Invitrogen) supplemented with 10 ng/ml M-CSF (Milteny) and 10 ng/ml interleukin (IL)-3 (Peprotech)]. Medium was replaced after 5–7 days of plating. After 11 days, the supernatant was seeded in a RepCell dish or collagen-coated dishes containing culture medium supplemented with 10 ng/ml M-CSF for 3 days. Then, detached cells by incubation at 4 °C or trypsin were used as osteoclast precursors for flow cytometric analysis, osteoclast differentiation, and pit formation assay. For osteoclast differentiation assay, the detached osteoclast precursors were seeded ($1.5–4 \times 10^4$ cells per well in a 48-well plate) and treated with 50 ng/ml RANKL and 10 ng/ml M-CSF for 3 days. Tartrate-resistant acid phosphatase (TRAP)-positive MNCs (TRAP + MNCs, more than three nuclei) were counted [17, 18]. For pit formation assay, the detached osteoclast precursors were seeded onto dentin slices and cultured for 3 days in the presence of RANKL and M-CSF. Staining of resorption pits was performed as described previously [19]. All cells were removed by sonication and stained with 20 μg/ml WGA-lectin-peroxidase (Sigma-Aldrich) for 30 min. Bone slices were washed to remove unbound lectin, and DAB substrate was used to develop the stain.

Flow cytometry analysis

Single-cell suspensions were subsequently incubated with anti-CD16/CD32 for 10 min, followed by staining with brilliant violet-conjugated anti-CD11b (M1/70; eBioscience) in FACS buffer [1× phosphate-buffered saline (PBS), 4 % heat-inactivated fetal calf serum, and 2 mM EDTA] for 15 min. Stained cells were analyzed on a FACSCanto II Flow Cytometer (BD Biosciences). FACS data were statistically analyzed with FlowJo software (TreeStar).

Quantitative RT-PCR analysis

Total RNA and cDNA were prepared using the RNeasy mini kit (Qiagen) and Superscript III reverse transcriptase (Invitrogen) according to the manufacturer's instructions. Real-time reverse transcription-polymerase chain reaction (RT-PCR) was performed with a Thermal Cycler Dice Real Time System (Takara) using SYBR Premix EX Taq (Takara). The primer sequences were *Actb*, 5′-CTTCTA CAATGAGCTGCGTG-3′ and 5′-TCATGAGGTAGTCTG TCAGG-3′; *Acp5*, 5′-GGGAAATGGCCAATGCCAAA GAGA-3′ and 5′-TCGCACAGAGGGATCCATGAAGT T-3′; *Ctsk*, 5′-AGGCAGCTAAATGCAGAGGGTACA-3′ and 5′-ATGCCGCAGGCGTTGTTCTTATTC-3′; *Nfatc1*, 5′-GGTAACTCTGTCTTTCTAACCTTAAGCTC-3′ and 5′-GTGATGACCCCAGCATGCACCAGTCACAG-3′.

Scanning electron microscope observation of resorption pits

The dentin slices were dehydrated and coated with osmium. The coated dentin slices were analyzed on a scanning electron microscope (S-4800; Hitachi).

Results

To induce osteoclasts from ESCs and iPSCs, we developed a three-step monoculture approach that involves mesoderm induction (step 1), fate specification to monocyte/macrophage lineage (step 2), and differentiation to functional osteoclasts (step 3) (Fig. 1a). Following detachment of ESCs and iPSCs from MEFs, ESCs and iPSCs aggregate in suspension cultures to form structures known as EBs (Fig. 1b), which are composed of cells from all three germ layers. Commitment to monocyte/macrophage lineage was achieved in media supplemented with M-CSF and IL-3. Three days after treatment of the supernatant with M-CSF, attached cells consisted of a single homogeneous cell population based on morphology (Fig. 1b) and highly expressed CD11b, which is a marker for osteoclast precursors [20] (Fig. 2).

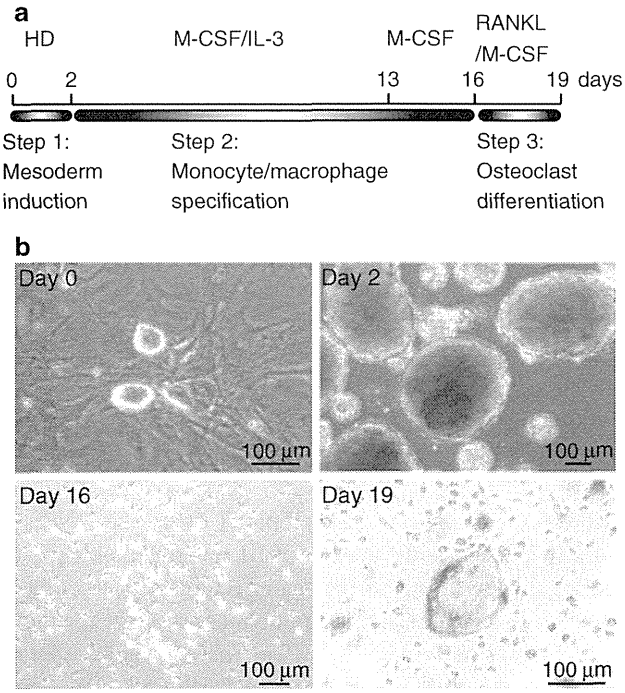

Fig. 1 A three-step method for differentiation of osteoclast-like cells from embryonic stem cells (ESCs) and induced pluripotent stem cells (iPSCs). **a** A schematic of the stepwise protocol used for the differentiation of ESCs (J1) and iPSCs (38c2 and 20D17) to the osteoclast lineage. **b** For embryoid body (EB) formation (**a**, Step 1), ESCs and iPSCs (*upper left*) on MEFs were trypsinized. After suspension in EB media, following conventional hanging-drop (HD) methods, EBs were produced from ESCs or iPSCs (*upper right*). For differentiation (**a**, Step 2), EBs were cultured under the presence of macrophage-colony stimulating factor (M-CSF) and interleukin 3 (IL-3). The supernatant containing monocyte/macrophage precursor-like cells was cultured under the presence of M-CSF, producing osteoclast precursors (*lower left*). Then, osteoclast precursors were used for osteoclast differentiation, pit formation, and FACS analysis. For osteoclast differentiation assay, the osteoclast precursors were seeded and treated with RANKL and M-CSF. Three days after treatment with RANKL, cells differentiated to TRAP-positive multinucleated cells (*lower right*)

Next, we investigated whether the osteoclast precursors derived from ESCs and iPSCs have the potential to differentiate further into functional osteoclasts. ESC-derived and iPSC-derived osteoclast precursors were detached and the cells cultured in the presence of RANKL and M-CSF, which are essential cytokines for osteoclast differentiation and survival [7, 21]. Three days after RANKL stimulation, large multinucleated cells (MNCs) formed in culture from ESCs and iPSCs (Figs. 1b, 3). These MNCs stained positively for TRAP, which is a enzyme highly expressed in osteoclasts [18, 22]. We estimated the efficiency of osteoclast differentiation (calculated as TRAP-positive MNCs divided by the total number of cells, consisting of TRAP-positive MNCs and NCs, and TRAP-negative cells). As the result, 4.0 ± 0.5 % of ESC-derived osteoclast precursors formed TRAP-positive MNCs, and 2.9 ± 0.5 and 4.0 ± 0.7 % of osteoclast precursors derived from 38c2 and 20D17 cell lines, respectively, differentiated into osteoclast-like cells.

To investigate whether multinucleated cells derived from ESCs and iPSCs have bone-resorbing activity, osteoclast precursors derived from ESCs and iPSCs were cultured on a mineralized dentine slice in the presence of RANKL and M-CSF. Analysis of pits demonstrated that both ESC-derived and iPSC-derived osteoclast-like cells were active and formed extensive resorption lacunae and trails (Fig. 4).

To characterize ESC-derived and iPSC-derived osteoclast-like cells using molecular markers, we checked the expression of osteoclast-specific genes. Quantitative PCR analysis showed that both ESC-derived and iPSC-derived cells expressed osteoclastic transcription factor, *Nfatc1*, and the osteoclast-specific enzymes, *Ctsk* and *Acp5* [7, 22], in a RANKL-dependent manner (Fig. 5).

Discussion

This study is the first to show a method for differentiation of mouse ESCs and iPSCs into bone-resorbing osteoclasts based upon a monoculture approach. The osteoclast, which is differentiated from monocyte/macrophage precursors [7, 20], is derived from hematopoietic stem cells of mesodermal origin [23]. In analogous fashion, our procedure consists of three steps involving mesoderm formation, commitment to hematopoietic lineage, and enrichment of precursor cells in the monocyte/macrophage lineage, and then osteoclast differentiation, suggesting that our approach is to mimic in vitro the natural sequence of osteoclast development in vivo. However, because recent studies have demonstrated that CD11b(−/low)B220

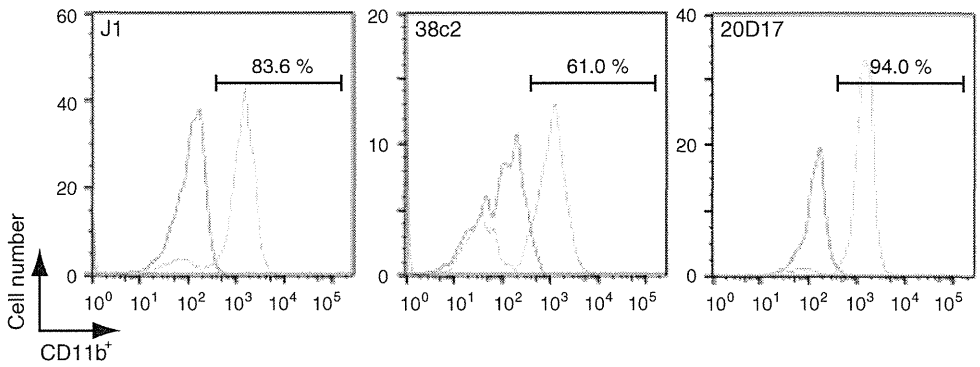

Fig. 2 CD11b surface expression on osteoclast precursors from ESCs and iPSCs shown by flow cytometric analysis of ESC-derived and iPSC-derived osteoclast precursors at day 16. *Blue* histograms represent population stained with anti-CD11b antibody and *red* histograms represent unstained control sample

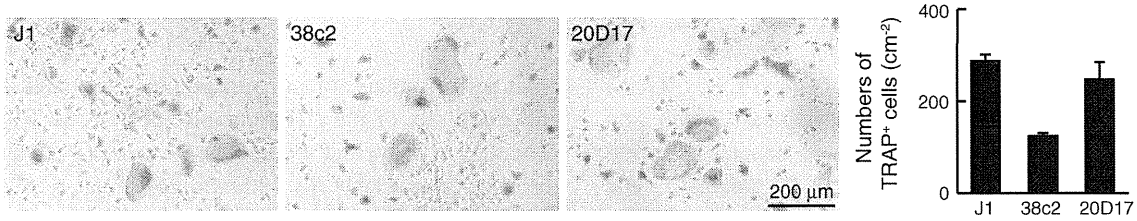

Fig. 3 Differentiation of osteoclast-like cells from ESCs and iPSCs shown by representative images of ESC-derived and iPSC-derived osteoclast-like cells at day 19. TRAP-positive multinucleated cells (more than three nuclei) were counted. Data represent mean ± SEM of three to six images

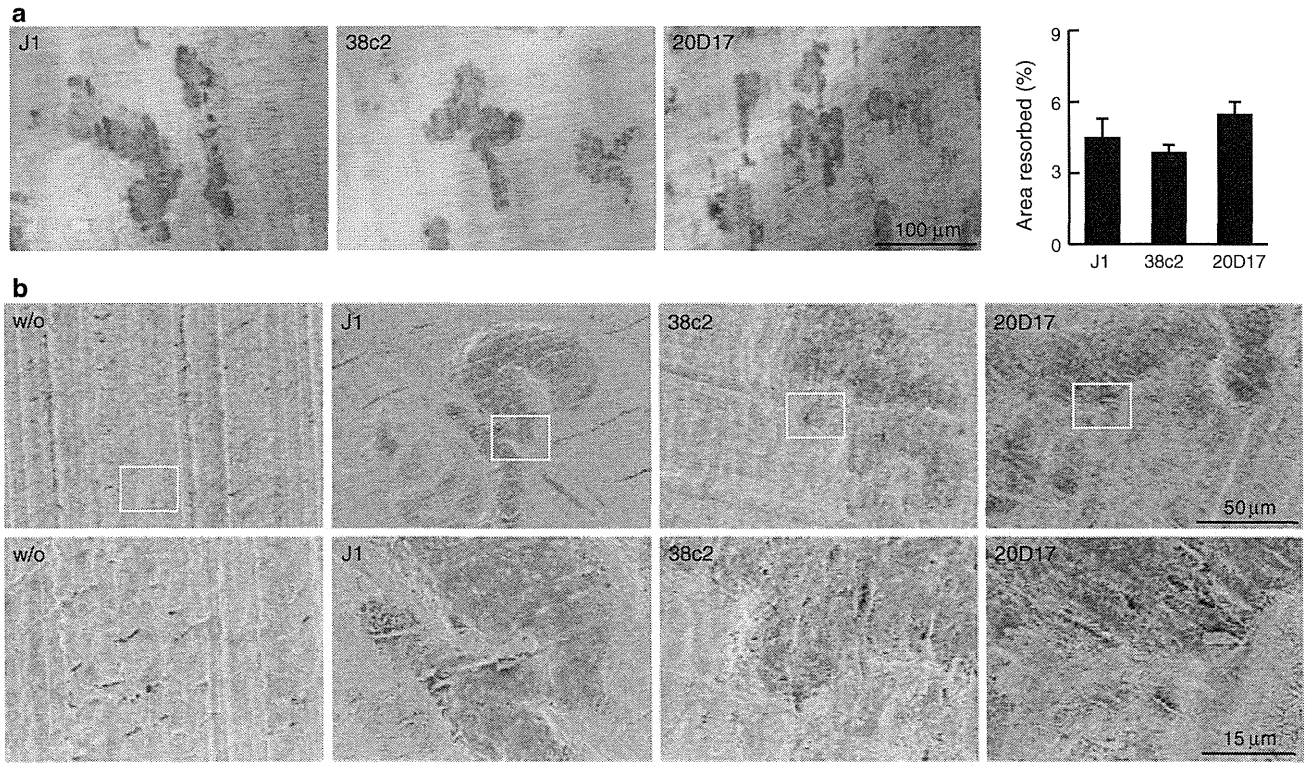

Fig. 4 Bone resorption by ESC-derived and iPSC-derived osteoclast-like cells. **a** Resorption lacunae created by ESC-derived and iPSC-derived osteoclast-like cell at day 19 were identified after removal of cells and staining with lectin-peroxidase. Area of resorption was measured. **b** Scanning electron microscope images of resorption lacunae. *Yellow boxed* regions in the *upper panels* are magnified in the *lower panels*. Data represent mean ± SEM of three to six images

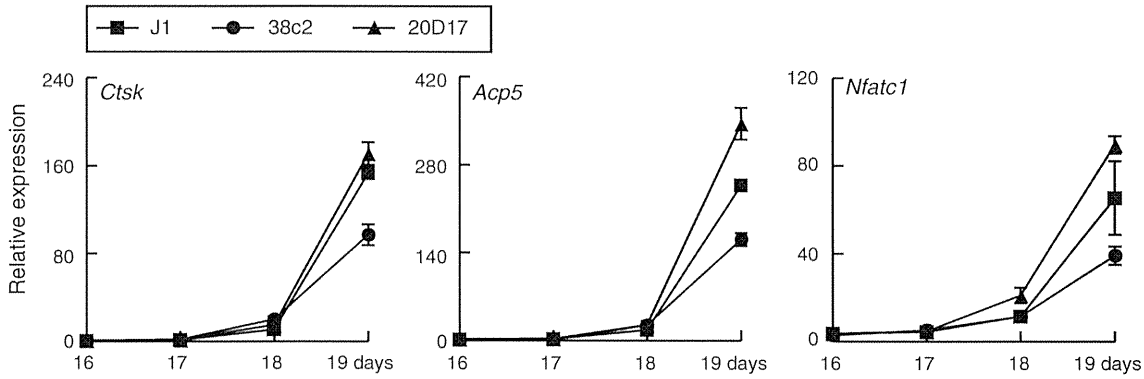

Fig. 5 Expression of osteoclast-specific genes in ESC-derived and iPSC-derived osteoclast-like cells. RANKL-dependent expression of osteoclast marker genes in cultures of ESCs and iPSCs-derived osteoclast precursors at day 16. Data represent mean ± SEM of three samples

(−)CD3(−)CD115(+) and CD11b(−/low)CX3CR1(+) Ly6C(high) cells are identified as osteoclast precursors in vivo [24, 25], further investigation is needed to investigate whether in vitro-generated osteoclast precursor cells contain these populations. In contrast, the reprogramming of fibroblasts into functional differentiated cells such as chondrocytes, neurons, and cardiomyocytes without first passing the cells through a pluripotent state has been reported [26, 27]. Potential advantage of direct reprogramming is the overall speed and simplicity of the differentiation conditions in comparison to the use of ESCs and iPSCs. However, currently available antiresorptives such as anti-RANKL antibody, cathepsin inhibitor, and bisphosphonates target different cellular processes such as differentiation, function, and survival, respectively [21, 28]. Therefore, stepwise differentiation protocol rather than direct reprogramming would be useful to investigate the mechanism of drug action.

Here, we describe an osteoclast differentiation protocol that efficiently differentiates iPSCs. In this study, we used two iPSC cell lines whose efficiency of TRAP-positive MNC formation has variability. As it has been reported that the efficiency is dependent on the cell origin [29, 30], an improved method to reset the epigenetic memory of donor-derived somatic cells may be required. However, based on our protocols, bone-resorbing osteoclasts were comparably produced in a iPSC cell line-independent manner. Accordingly, the fact that the protocol works well with the disparate iPSC lines demonstrates the potential of a universal differentiation protocol for bone-resorbing osteoclasts.

An important but unsolved question in this study is whether our approach is applicable for the differentiation of human ESCs and iPSCs to bone-resorbing osteoclasts. Although recent studies have demonstrated the direct differentiation of human ESCs and iPSCs to multipotential myeloid precursors and further differentiation to multinucleated osteoclasts that exhibit resorptive capacity [31], the potential advantage of our procedure is the overall speed and simplicity of the differentiation conditions. Therefore, we could improve the method for generating human bone-resorbing osteoclasts from human ESCs and iPSCs on the basis of our procedure.

Acknowledgments We thank H. Omori and N. Furukawa for help and discussion. This work was supported by Grant-in-Aids for Creative Scientific Research and Young Scientist (A) from the Japan Society for the Promotion of Science (JSPS); Grant-in-Aid for Challenging Exploratory Research from the JSPS; and grants from the Nakajima Foundation, the Mochida Memorial Foundation for Medical and Pharmaceutical Research, Astellas Foundation for Research on Metabolic Disorders and Takeda Science Foundation.

Conflict of interest All authors state that they have no conflicts of interest.

References

1. Keller G (2005) Embryonic stem cell differentiation: emergence of a new era in biology and medicine. Genes Dev 19:1129–1155
2. Kiskinis E, Eggan K (2010) Progress toward the clinical application of patient-specific pluripotent stem cells. J Clin Invest 120:51–59
3. Hemmi H et al (2001) Temporal and spatial localization of osteoclasts in colonies from embryonic stem cells. Biochem Biophys Res Commun 280:526–534
4. Takayanagi H et al (2002) Induction and activation of the transcription factor NFATc1 (NFAT2) integrate RANKL signaling in terminal differentiation of osteoclasts. Dev Cell 3:889–901
5. Tsuneto M, Yamazaki H, Yoshino M, Yamada T, Hayashi S (2005) Ascorbic acid promotes osteoclastogenesis from embryonic stem cells. Biochem Biophys Res Commun 335:1239–1246
6. Goodman ML, Chen S, Yang FC, Chan RJ (2009) Novel method of murine embryonic stem cell-derived osteoclast development. Stem Cells Dev 18:195–200
7. Takayanagi H (2007) Osteoimmunology: shared mechanisms and crosstalk between the immune and bone systems. Nat Rev Immunol 7:292–304
8. Lorenzo J, Horowitz M, Choi Y (2008) Osteoimmunology: interactions of the bone and immune system. Endocr Rev 29:403–440

9. Goldring SR, Gravallese EM (2000) Mechanisms of bone loss in inflammatory arthritis: diagnosis and therapeutic implications. Arthritis Res 2:33–37
10. Kong YY et al (1999) Activated T cells regulate bone loss and joint destruction in adjuvant arthritis through osteoprotegerin ligand. Nature (Lond) 402:304–309
11. Takayanagi H et al (2000) T-cell-mediated regulation of osteoclastogenesis by signalling cross-talk between RANKL and IFN-γ. Nature (Lond) 408:600–605
12. Rodan GA, Martin TJ (2000) Therapeutic approaches to bone diseases. Science 289:1508–1514
13. Landesberg R et al (2011) Potential pathophysiological mechanisms in osteonecrosis of the jaw. Ann N Y Acad Sci 1218:62–79
14. Orozco C, Maalouf NM (2012) Safety of bisphosphonates. Rheum Dis Clin N Am 38:681–705
15. Li E, Bestor TH, Jaenisch R (1992) Targeted mutation of the DNA methyltransferase gene results in embryonic lethality. Cell 69:915–926
16. Okita K, Ichisaka T, Yamanaka S (2007) Generation of germline-competent induced pluripotent stem cells. Nature (Lond) 448:313–317
17. Nishikawa K et al (2010) Maf promotes osteoblast differentiation in mice by mediating the age-related switch in mesenchymal cell differentiation. J Clin Invest 120:3455–3465
18. Hayashi M et al (2012) Osteoprotection by semaphorin 3A. Nature (Lond) 485:69–74
19. Selander K, Lehenkari P, Vaananen HK (1994) The effects of bisphosphonates on the resorption cycle of isolated osteoclasts. Calcif Tissue Int 55:368–375
20. Ishii M et al (2009) Sphingosine-1-phosphate mobilizes osteoclast precursors and regulates bone homeostasis. Nature (Lond) 458:524–528
21. Tanaka S, Nakamura K, Takahasi N, Suda T (2005) Role of RANKL in physiological and pathological bone resorption and therapeutics targeting the RANKL-RANK signaling system. Immunol Rev 208:30–49
22. Nishikawa K et al (2010) Blimp1-mediated repression of negative regulators is required for osteoclast differentiation. Proc Natl Acad Sci USA 107:3117–3122
23. Dzierzak E, Speck NA (2008) Of lineage and legacy: the development of mammalian hematopoietic stem cells. Nat Immunol 9:129–136
24. Charles JF et al (2012) Inflammatory arthritis increases mouse osteoclast precursors with myeloid suppressor function. J Clin Invest 122:4592–4605
25. Jacome-Galarza CE, Lee SK, Lorenzo JA, Aguila HL (2013) Identification, characterization, and isolation of a common progenitor for osteoclasts, macrophages, and dendritic cells from murine bone marrow and periphery. J Bone Miner Res 28:1203–1213
26. Hiramatsu K et al (2011) Generation of hyaline cartilaginous tissue from mouse adult dermal fibroblast culture by defined factors. J Clin Invest 121:640–657
27. Chambers SM, Studer L (2011) Cell fate plug and play: direct reprogramming and induced pluripotency. Cell 145:827–830
28. Asagiri M et al (2008) Cathepsin K-dependent toll-like receptor 9 signaling revealed in experimental arthritis. Science 319:624–627
29. Polo JM et al (2010) Cell type of origin influences the molecular and functional properties of mouse induced pluripotent stem cells. Nat Biotechnol 28:848–855
30. Kim K et al (2010) Epigenetic memory in induced pluripotent stem cells. Nature (Lond) 467:285–290
31. Grigoriadis AE et al (2010) Directed differentiation of hematopoietic precursors and functional osteoclasts from human ES and iPS cells. Blood 115:2769–2776